



## RESEARCH ARTICLE

10.1002/2015JC011381

## Influence of bubble size, diffuser width, and flow rate on the integral behavior of bubble plumes

Bruño Fraga<sup>1</sup> and Thorsten Stoesser<sup>1</sup><sup>1</sup>Hydro-Environmental Research Centre, Cardiff School of Engineering, Cardiff University, Cardiff, UK

## Special Section:

Physical Processes  
Responsible for Material  
Transport in the Gulf of  
Mexico for Oil Spill  
Applications

## Key Points:

- Large-eddy simulation of bubble plumes
- Assessment of integral bubble plume properties and coefficients/assumptions
- Effect of the bubble size on the plume's structure and entrainment rate

## Correspondence to:

B. Fraga,  
FragaB@cardiff.ac.uk

## Citation:

Fraga, B., and T. Stoesser (2016), Influence of bubble size, diffuser width, and flow rate on the integral behavior of bubble plumes, *J. Geophys. Res. Oceans*, 121, 3887–3904, doi:10.1002/2015JC011381.

Received 8 OCT 2015

Accepted 4 MAY 2016

Accepted article online 9 MAY 2016

Published online 4 JUN 2016

© 2016. The Authors.

Journal of Geophysical Research: Oceans published by Wiley Periodicals, Inc. on behalf of American Geophysical Union.

This is an open access article under the terms of the Creative Commons Attribution-NonCommercial-NoDerivs License, which permits use and distribution in any medium, provided the original work is properly cited, the use is non-commercial and no modifications or adaptations are made.

**Abstract** A large-eddy simulation based Eulerian-Lagrangian model is employed to quantify the impact of bubble size, diffuser diameter, and gas flow rate on integral properties of bubble plumes, such as the plume's width, centerline velocity, and mass flux. Calculated quantities are compared with experimental data and integral model predictions. Furthermore, the LES data were used to assess the behavior of the entrainment coefficient, the momentum amplification factor, and the bubble-to-momentum spread ratio. It is found that bubble plumes with constant bubble size and smaller diameter behave in accordance with integral plume models. Plumes comprising larger and non-uniform bubble sizes appear to deviate from past observations and model predictions. In multi-diameter bubble plumes, a bubble self-organisation takes place, i.e., small bubbles cluster in the center of the plume whilst large bubbles are found at the periphery of the plume. Multi-diameter bubble plumes also feature a greater entrainment rate than single-size bubble plumes, as well as a higher spread ratio and lower turbulent momentum rate. Once the plume is fully established, the size of the diffuser does not appear to affect integral properties of bubble plumes. However, plume development is affected by the diffuser width, as larger release areas lead to a delayed asymptotic behavior of the plume and consequently to a lower entrainment and higher spread ratio. Finally, the effect of the gas flow rate on the integral plume is studied and is deemed very relevant with regards to most integral plume properties and coefficients. This effect is already fairly well described by integral plume models.

## 1. Introduction

Buoyant plumes are quite common multiphase flows in the environment, e.g., hydrothermal vents or submarine springs. Engineering applications of bubble plumes include destratification and aeration of lakes or reservoirs, creation of silt curtains, inhibitors of ice formation/salt intrusions, or injection of CO<sub>2</sub> in the deep ocean. Gas plumes usually occur in underwater blow-outs of oil wells too [e.g., *Fabregat et al.*, 2015; *Socolofsky and Adams*, 2003; *Yapa et al.*, 1999]. Due to their complexity and wide-reaching applications, there is strong scientific interest in understanding the detailed fluid mechanics in this kind of multiphase flow [*Mazzitelli and Lohse*, 2009], however, only few detailed experimental studies exist [e.g., *Martinez Mercado et al.*, 2010; *Seol et al.*, 2007]. This work uses large-eddy simulation to expand the parameter range of bubble plumes complementing physical modeling.

Experiments have provided the input to the development of integral plume models based on semi-empirical equations. Integral plume models are employed regularly in science and engineering to predict the behavior of plumes. For instance, mixing and dilution models such as USEPA's "Visual Plumes" or the well-known "Comix" model are based on integral plume model outputs. Other examples are the oil-spill trajectory models which utilize integral plume equations for the provision of boundary conditions, such as the one employed by *North et al.* [2011] to predict the fate of the spilled oil from the Deepwater Horizon blowout.

*Kobus* [1968] and *Cederwall and Ditmars* [1970] developed the first generation of such integral models by adapting existing models for single-phase plumes [*Morton et al.*, 1956] to multiphase plumes by incorporating the slip velocity, i.e., the difference in velocity between the two phases. *Milgram* [1983] provided valuable experimental data to verify these models and also investigated in depth the models' main parameters: the entrainment coefficient, the bubble-to-velocity spread ratio, and the momentum amplification factor. *Buscaglia et al.* [2002] verified the integral approach from a theoretical point of view by averaging the three-dimensional equations of motion of a mixed fluid. In order to address the problem of not-solving the near-field recirculating flow around the plume, *Mcdougall* [1978] introduced the idea of the double plume in

1978, which was then followed, improved, and generalized by *Asaeda and Imberger* [1993], *Crouse* [2000], *Socolofsky and Adams* [2002], or *Socolofsky et al.* [2008] among others. *Wüest et al.* [1992] developed a discrete bubble model for reservoirs in which the properties were evaluated in one bubble and extended to the rest at the same height. This model was used successfully in unstratified and stratified conditions by *McGinnis and Little* [2002] and *McGinnis et al.* [2004].

The constant increase in computational resources enables more sophisticated modeling/simulation of bubbly flows albeit not at very large scales such as the Deepwater Horizon blow-out plume. Three-dimensional numerical modeling/simulation requires the solution of the equations of motion for the carrier and dispersed phases as well as the coupling and interaction between the two and this requires substantial computational resources. The first challenge to overcome is the accurate prediction of the turbulence in the carrier phase, for which three main approaches exist: (1) numerical resolution of all turbulent scales, i.e., Direct Numerical Simulation (DNS), (2) explicit numerical resolution of the larger and more energetic scales and subgrid-scale modeling of the small scales, i.e., large-eddy simulation (LES), or (3) modeling of the entire turbulence spectrum through a turbulence model and solving for the time-averaged flow only, i.e., Reynolds-Averaged Navier-Stokes simulation (RANS). RANS simulations rely on closure models to account for the unsteadiness in the flow and this approach is the computationally least demanding of the three. On the other hand, bubbles induce significant turbulence (also called pseudoturbulence) of anisotropic nature even at low Reynolds numbers [*Dhotre et al.*, 2013], which RANS models cannot represent accurately. DNS is the most accurate approach to predict bubble plume dynamics, but its high cost prevents it from being employed for many practical applications. LES appears to be a promising compromise between accuracy and applicability [*Stoesser*, 2014] in engineering. The second challenge modeling approaches face is the accurate treatment of the dispersed phase and its coupling. Three alternatives exist: (1) Eulerian-Eulerian (EE), i.e., both the carrier phase and the gas phase are computed in an Eulerian framework [e.g., *Deen et al.*, 2001; *Dhotre et al.*, 2009; *Fabregat et al.*, 2015; *Milelli et al.*, 2001; *Ničeno et al.*, 2009; *Sokolichin et al.*, 1997], (2) Eulerian-Lagrangian (EL), i.e., the carried liquid is calculated as in (1) and the gas phase is treated as Lagrangian markers, and (3) Interface Tracking (IT), i.e., the carried liquid is calculated as in (1) and the interface between liquid and gas phases are resolved by the numerical method [see *Bunner and Tryggvason*, 2002; *Esmaeli and Tryggvason*, 1998; *Lu et al.*, 2005; *Roghair et al.*, 2011; *Yujie et al.*, 2012]. In theory, all turbulence treatments can be combined with the approaches of the dispersed phase; however, due to the inherent very high resolution of the Interface Tracking approach (10–20 grid points per bubble), IT is almost always automatically a DNS.

In Eulerian-Lagrangian-based models, each bubble is represented by a Lagrangian point which moves freely across the Eulerian domain according to Newton's second law of motion. The EL approach is most often combined with RANS and more recently with LES. Compared to EE, EL gives detailed information about every bubble's position, force, and velocity, together with adequately resolved large and medium-scale turbulence. On the other hand, EL is more expensive than EE because each particle requires the calculation of a set of equations and a mapping procedure between the Lagrangian and Eulerian coordinates. Compared to IT, EL is less costly (lower resolution, broader assumptions) and offers wider applicability, being able to deal with much larger number of particles and higher Reynolds numbers (most IT simulations are constrained to low  $Re$  and no more than 250 bubbles at any time). On the other hand, in EL, the bubble-liquid interface is not resolved and the method relies on semiempirical formulae to compute acting bubble forces. Some successful examples of large-eddy simulation of bubble plumes using an Lagrangian Particle Tracking (LPT) algorithm are: *Darmana et al.* [2006], *Deen et al.* [2004], *Delnoij et al.* [1997], *Hu and Celik* [2008], *Kitagawa et al.* [2001], and *Sungkorn et al.* [2011]. Sophisticated EL-LES approaches have been employed recently to predict accurately the fluid mechanical details of bubble plumes [e.g., *Fraga et al.*, 2016; *Hu and Celik*, 2008] and their outputs can be used to inform integral plume models. The overarching objective of this study is to employ a fully validated EL-LES to investigate the effect of various plume parameters on the integral behavior of bubble plumes. Parameters investigated are: bubble size, diffuser width, and gas flow rate. Furthermore, the study discusses the applicability and reliability of the underlying empirical coefficients used by integral plume models.

## 2. Integral Plume Models and Scaling

Integral plume models are based on the main assumption of self-similarity and the hypothesis of entrainment. The latter is a consequence of the former, as the prediction of a linear spread of the plume radius

with height already establishes a nonexplicit relation between the vertical momentum flux and the radial velocities [Turner, 1986]. These models have been very successful in providing accurate predictions of integral properties of the plume, such as the centerline velocity, plume’s width, and volume flux among others. They are based on the integration of the basic conservation laws of mass and momentum together with assumptions mainly regarding the entrainment and recirculation processes. The integral models’ simplicity allows them to provide very quick predictions for real-scale plumes. However, integral models have several disadvantages and limitations: they are unable to predict the individual behavior of bubbles, they do not explicitly solve the fluxes occurring in radial or lateral planes (the entrainment assumption is used instead), and they do not provide information regarding turbulence and second-order statistics. They also rely on empirical parameters, such as the spread ratio  $\lambda$ , the momentum amplification coefficient  $\gamma$ , and the entrainment coefficient  $\alpha$ , which have been obtained from and confirmed by a limited number of laboratory experiments.

The derivation of empirical parameters and constants requires adequate scaling. The characteristic velocity in the plume is usually the slip velocity,  $w_{slip}$ , i.e., the difference between gas and liquid velocities at a particular location. The characteristic length,  $D$ , is given by [Bombardelli et al., 2007]:

$$D = \frac{gQ_g}{4\pi\alpha^2 w_{slip}^3} \tag{1}$$

where  $g$  is the gravity acceleration and  $Q_g$  the gas flow rate. Another relevant parameter is the densimetric bubble Froude number  $F$ , which was introduced by Wüest et al. [1992]:

$$F = \frac{w}{[2\lambda b_w g(\rho_a - \rho_m) / \rho_m]^{1/2}} \tag{2}$$

where  $\rho_a$  is the density of air,  $\rho_m$  the density of the air-water mixture, and  $w$  a characteristic plume velocity. Given a diffuser width  $b_w = b_0$  and empirical values of the densimetric bubble Froude number measured at the diffuser ( $F_0$ ), equation (2) provides the initial velocity  $w_0$  for integral models. Bombardelli [Bombardelli et al., 2007] used the scaling relations to define three different regions in the plume: the “asymptotic zone,” i.e.,  $z > 5D$ , which is insensitive to the initial conditions, the “adjustment zone,” i.e., between the diffuser and  $z \cong 10b_0$ , which is characterized by a constant  $F$ , and an “intermediate zone” between the other two in which  $F$  is not constant but the influence of the diffuser diameter is still relevant. Normally,  $5D > 10b_0$ , but in the case of  $b_0 > 0.5D$ , the adjustment and intermediate zones will extend beyond  $5D$ . Despite the well-contrasted adequacy of the aforementioned parameters, scaling for bubble plumes still presents some deficits which inherently limit the accuracy of integral models which are the lack of scaling relations for turbulence statistics, no clear scaling procedures for horizontal distances, or uncertainty regarding the influence of different bubble sizes [Bombardelli et al., 2007].

### 3. Numerical Framework

In this study, the in-house finite difference-based large-eddy simulation code Hydro3D is employed. Hydro3D solves the filtered Navier-Stokes equations on a staggered grid for the continuous (liquid) phase and has been validated thoroughly for many different flows [e.g., Bomminayuni and Stoesser, 2011; Bai et al., 2013; Kara et al., 2012, 2015; Kim and Stoesser, 2011; Kim et al., 2013; Papanicolaou et al., 2012]. The code is equipped with a Lagrangian Particle Tracking algorithm to allow for accurate predictions of the dispersed (bubbles) phase. A detailed model description of this approach can be found in Fraga et al. [2016].

#### 3.1. Continuous Phase

Hydro3D solves the space-filtered mass and momentum conservation equations for an incompressible fluid:

$$\frac{\partial u_i}{\partial x_i} = 0 \tag{3}$$

$$\frac{\partial u_i}{\partial t} + \frac{\partial u_i u_j}{\partial x_j} = -\frac{\partial p}{\partial x_i} + 2\nu \frac{\partial(S_{ij})}{\partial x_j} - \frac{\partial \tau_{ij}}{\partial x_j} + 2g\delta_{i,3} + \xi_i \quad (4)$$

where  $u_i$  refers to the filtered velocity component in the spatial direction  $i$ ,  $t$  is the time,  $p$  the filtered pressure,  $\nu$  the dynamic viscosity, and  $S_{ij}$  the strain rate tensor. The term  $\tau_{ij}$  accounts for the unresolved, subgrid-scale (SGS) turbulence, which is calculated through the turbulent viscosity  $\nu_t$  using the Smagorinsky SGS model. The Smagorinsky constant  $C_s$  is set to  $C_s=0.1$  for all simulations.  $\xi_i$  is a source term and accounts for the contribution of the dispersed phase to the liquid phase momentum. The derivatives in the governing equations are discretized with a three-step Runge-Kutta algorithm for the time derivative and second-order central differencing schemes for both convective and diffusive terms. The code is based on a predictor-corrector fractional step method with the solution of the Poisson pressure equation using a multigrid method as the corrector.

### 3.2. Dispersed Phase

The bubbles are represented by volumeless Lagrangian points/markers. The physical effect of the liquid-gas mixture is accounted for through forcing terms to be described in this section. The assumptions made are: (i) the bubbles are rigid and spheric and (ii) there is no direct interaction between them (due to the relatively dilute gas mixture). Also, only linear interaction between interfacial forces is considered. The motion of individual bubbles (from here onward called particles) is computed by Newton's second law:

$$m_p \frac{\partial u_{p,i}}{\partial t} = F_{p,i} \quad (5)$$

where  $m_p$  is the particle's mass,  $u_{p,i}$  is the particle's velocity in spatial direction  $i$ , and  $F_{p,i}$  is the sum of the interfacial liquid forces acting on the particle in direction  $i$ . The integral forces acting on each particle are approximated by semiempirical formulae. According to the most commonly accepted formulation [Delnoij *et al.*, 1997], five forces are considered: buoyancy, fluid stress, added mass, drag, and lift. The expressions for each force are detailed in Fraga *et al.* [2016] and should not be repeated for brevity. These forces are calculated based on the size of the bubble, its velocity on the previous time step, and the velocity field of the surrounding liquid. By substituting the force equations into equation (5), the following explicit formula for the particle velocity is obtained:

$$u_{p,i}^t = u_{p,i}^{t-1} + \Delta t \left[ 2g\delta_{i,3} + 3 \frac{W_{slip}}{\Delta t} - \frac{3}{2D_p} C_d |W_{slip}| W_{slip} - 2C_L W_{slip} \times \omega_i^{t-1} \right] \quad (6)$$

where  $t$  is time,  $D_p$  is the bubble diameter,  $C_d$  and  $C_L$  are the drag and lift coefficients, respectively, and  $\omega_i$  is the vorticity component in the  $i$  direction. The term  $2g$  accounts for the buoyancy force and only acts in the vertical direction ( $i = 3$ ).

### 3.3. Eulerian-Lagrangian Coupling

In a two-way coupling approach, as it is proposed here, exchange of information is required twice. First, the interfacial particle forces are calculated and the particles' velocities obtained through equation (6). This is called forward coupling. Second, the contribution of the dispersed phase to the continuous phase is computed and added as a source term,  $\xi_i$ , to the liquid's momentum equations (4). This is called reverse or backward coupling. Forward and backward coupling are achieved by connecting randomly placed Lagrangian particles with fixed locations of the Eulerian framework and this is achieved through a mapping technique. The model employed herein is a modified version of the PSI-ball concept by Hu and Celik [2008] developed by Fraga *et al.* [2016]: the region of space inside which a bubble influences an Eulerian node (and vice versa) is a cube whose dimensions depend on  $D_p/\Delta x$ , the ratio between the bubble diameter and the grid size. This procedure ensures that the number of nodes/markers considered for the interpolation is representative and independent of the relative size of the bubble. For the forward coupling, the interpolation and/or transfer of quantities between phases is done through the smoothed delta functions developed by Yang *et al.* [2009]. Delta functions require the collection of points to be regularly arranged, which is not the case of the bubbles within the gas plume. Hence, for the backward coupling, a volume-average is applied, during which the contribution of every particle over an Eulerian node is multiplied by a term  $\Delta V = \frac{V_p}{V_{ball}} \frac{L_j}{L_k}$ , being  $V_p$  the volume of the bubble and  $V_{ball}$  the volume of the influence region and  $\frac{L_j}{L_k}$  is a distance weighted linear

function that ensures those particles which are closer to the considered node have a bigger impact. The momentum source term  $\xi_j$  is computed as:

$$\xi_j = -\frac{1}{V_p} \sum_{p=1}^M F_{p,i}^* \Delta V \quad (7)$$

where  $M$  is the number of bubbles influenced by a certain number of fluid nodes. The backward forcing term  $F_{p,i}^*$  is obtained in an analogous way to the forward one, except that in this case, the buoyancy force is not included, as the effect of the buoyancy on the liquid phase is already specified in the momentum equations (see equation (4)) for  $i = 3$ :

$$F_{p,i}^* = F_{D,i}^* + F_{L,i}^* + F_{S,i}^* + F_{A,i}^* \quad (8)$$

where  $F_{D,i}^*$ ,  $F_{L,i}^*$ ,  $F_{S,i}^*$ , and  $F_{A,i}^*$  are the drag, lift, fluid stress, and added mass backward forces. As this is an explicit approach, these backward forces are calculated using the particles' velocities of the current time step  $u_{p,i}^t$  (calculated in equation (6)), whereas the forward forcing formulation is based on the previous time step's velocity  $u_{p,i}^{t-1}$ .

### 3.4. Calculating Integral Properties and Coefficients

The LES results are used to determine the main outputs provided by integral plume models and the three main empirical coefficients used in these models. The LES-predicted velocity radius of the plume is based on the self-similar assumption:

$$W(b_w) = e^{-1} W_c \quad (9)$$

where  $b_w$  is the half width of the plume at a given depth and  $W_c$  the vertical velocity at the center of the plume. The LES prediction is compared with *Rouse et al.*'s [1952] equation which calculates  $b_w$  as:

$$\frac{b_w}{D} = 0.11 \frac{z}{D} \quad (10)$$

The LES-predicted vertical velocity in the center of the plume,  $W_c$ , is compared with *Bombardelli et al.*'s [2007] model:

$$\frac{W_c}{W_{slip}} = \left( \frac{1.9 \left(\frac{z}{D}\right)^{-1}}{1 + 0.563 \left(\frac{z}{D}\right)^{\frac{1}{2}}} \right) \quad (11)$$

The mass flux transported by the plume is obtained by integrating radially the LES data. The result is compared with the following equation, which is a combination of equations (10) and (11):

$$\frac{Q}{W_{slip} D^2} = \pi \left( 0.11 \frac{z}{D} \right)^2 \left( \frac{1.9 \left(\frac{z}{D}\right)^{-1}}{1 + 0.563 \left(\frac{z}{D}\right)^{\frac{1}{2}}} \right) \quad (12)$$

The plume radius, centerline velocity, and mass flux predicted by the LES are also compared with five different sets of experimental data, which have been previously published in the following references: *Milgram* [1983], *Milgram and van Houten* [1982], *Fannelop and Sjoen* [1980], *Lai* [2015], and *Seol et al.* [2007].

The three coefficients of integral models discussed in the present paper are the entrainment coefficient,  $\alpha$ , the momentum amplification factor,  $\gamma$ , and the gas/velocity spread ratio,  $\lambda$ . An important physical aspect of plumes is their entrainment of ambient fluid. Integral plume models generally assume that the rate of lateral entrainment is a fraction of the centerline streamwise velocity at a certain depth. This fraction is represented by  $\alpha$ , which is generally considered to be a constant although it is known that it varies with depth in bubble plumes [*Socolofsky et al.*, 2002]. Once  $\alpha$  is known the lateral inflow (entrainment)  $E(z)$  is then calculated as:

$$E(z) = \alpha W_c(z) \quad (13)$$

Equation (13) is applied to calculate  $\alpha$  from the LES data. For a given height, the entrainment  $E(z)$  can be calculated by integrating along the perimeter of the plume the flux in the direction of the core at the radial

point  $r = b_w$ . Knowing the entrainment and the centerline velocity  $W_c(z)$ ,  $\alpha(z)$  can be determined. The resulting estimate is compared with *Seol et al.*'s [2007] algebraic model:

$$\alpha = 0.18 \exp\left(-\frac{1.7W_{slip}}{(B/z)^{1/3}}\right) + 0.04 \quad (14)$$

where  $B = g \left(\frac{\rho_w - \rho_g}{\rho_w}\right) \frac{H_A}{H_T} Q_g$  is the buoyancy flux, being  $\rho_w$  and  $\rho_g$  the water and gas densities, respectively,  $H_A$  the atmospheric pressure head and  $H_T = H_A + h$  the static pressure at the diffuser, being  $h$  the diffuser's depth.

The momentum amplification factor is the ratio of turbulence-driven momentum to the total momentum transport. It is calculated as:

$$\gamma = (\overline{w'w'} + \bar{W}^2) / \bar{W}^2 \quad (15)$$

where  $\overline{w'w'}$  is the turbulent stress in the vertical direction and  $\bar{W}$  is the time-averaged vertical velocity. As previous works have shown, the turbulent transport in the radial direction may constitute a significant part of the total momentum [e.g., *Fraga et al.*, 2016], hence an alternative formulation is also used in this work:  $\gamma = (\overline{w'w'} + \overline{u'u'} + \bar{W}^2) / \bar{W}^2$ , being  $u'$  the turbulent velocity fluctuation in the radial direction. This second approach intends to show the relative weight of the turbulence in the horizontal plane to the overall momentum transport. These two quantities are integrated over the radial plane of the plume to obtain the vertical distribution of  $\gamma$ .

The bubble-to-velocity spread ratio  $\lambda$  is the relation between the gas-containing plume radius  $b_g$  by the aforementioned velocity plume radius  $b_w$ . Measuring the width of the bubble core is not easy as there is not a standard definition of it (as there is for the velocity radius; see equation (9)) and the behavior of the bubble's core is yet not well understood [*Socolofsky et al.*, 2002]. Here it is computed as the time-averaged distance between plume centerline to the bubble furthest away from the center at a given height. The values of  $b_g$  so obtained are in agreement with the visualized plumes for every case.

## 4. Results and Discussion

### 4.1. Model Setup

The simulations reported here are an extension of the bubble plume that was studied experimentally in the Fluid Dynamics Laboratory in the Zachry Department of Civil Engineering at Texas A&M University [*Lai*, 2015]. In the experiments, compressed air was injected at a constant gas flow rate at standard conditions through an aquarium airstone located at the bottom of a 1 m wide, 1 m deep tank.

The numerical simulations are carried out under analogous geometrical conditions to the experiment. Bubbles are initially randomly distributed over the diffuser and once they make their way through the tank and reach the water surface they are removed from the computational domain. Boundary conditions for the continuous phase include the use of the no-slip boundary condition at all solid walls and a rigid lid at the water surface with a free slip condition. Grid size sensitivity was studied previously [*Fraga et al.*, 2016] for the laboratory experiment and suggests that a constant grid spacing of  $\Delta x = 3.125$  mm gives accurate predictions yielding a total of 32.7 Mio grid points for the entire domain. All the seven different simulations presented in this work follow this setup. They differ in the variation of three physical parameters: bubble size, diffuser width, and flow rate. Table 1 shows the dimensionless length ( $D$ ) and velocity ( $w_{slip}$ ) scales governing each of the seven scenarios and the average number of bubbles at any time in the tank. The slip velocity is calculated from the LES data and the results confirm that calculated  $w_{slip}$  agree well with the ones computed by the empirical relationships given in *Clift et al.* [1978]. The results were collected after a minimum simulation time equivalent to, at least, 5000 flow-throughs for every case.

### 4.2. Influence of the Bubble Size

The bubble size appears to be an important parameter in bubble plumes. First of all, it governs the magnitude of the driving forces, i.e., Buoyancy, Lift, Drag, Virtual Mass, and Fluid Stress, and second, it affects the dynamics of the plume, e.g., if gas flow rate is kept constant, it can be argued that a plume with fewer larger bubbles would behave differently than a plume composed of many smaller bubbles. The parameter bubble

**Table 1.** Velocity and Length Scales and Time-Averaged Number of Particles for the Seven Scenarios Considered

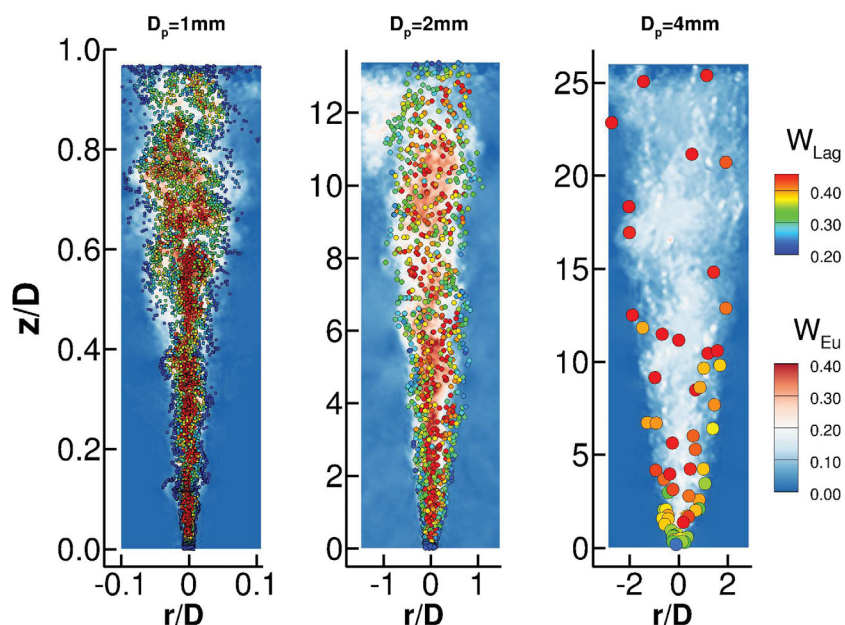
$Q_g$ (L/min)	$b_0$ (cm)	$D_p$ (mm)	$w_{slip}$ (cm/s)	$D$ (cm)	$N_p$
0.5	1.5	2	24	6.8	6,000
0.5	1.5	1	10	94	50,000
0.5	1.5	4	30	3.5	500
0.5	1.5	0.75–3.25	24	6.8	6,000
0.5	3	2	24	6.8	6,000
0.5	6	2	24	6.8	6,000
1.5	1.5	2	24	20.4	20,000

size has not received sufficient attention due to the fact that it is difficult for experimentalists to prescribe a specific bubble size. There are only few recent studies that attempted to address this issue by using different diffuser designs, crystal beads of various diameters or oil droplets, mostly in stratified environments [e.g., Chan et al., 2014; Bombardelli et al., 2007; Socolofsky and Adams, 2003, 2005].

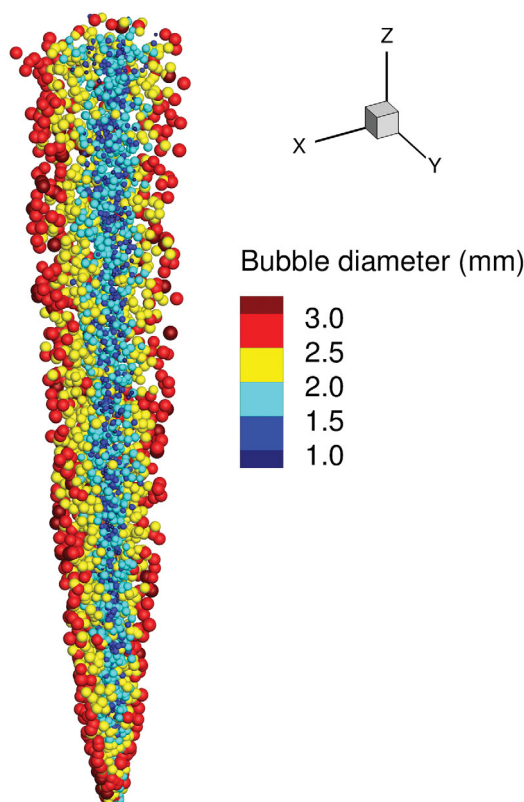
Three different cases with uniform bubble diameters of  $D_p = 1, 2,$  and  $4$  mm are tested, plus one more scenario with a random distribution of the diameter. A constant gas flow rate of  $Q_g = 0.5$  L/min and a  $1.5$  cm diffuser diameter is set for all the simulations, as stated in Table 1. The multisize (MS) case releases randomly sized bubbles according to a Gaussian distribution. As the average diameter of the MS case is  $D_p = 2$  mm, it is assumed that  $w_{slip} = 24$  cm/s and  $D = 6.8$  cm as in the uniform  $D_p = 2$  mm scenario.

Figure 1 shows snapshots of the three plumes at arbitrary instants in time. The bubbles are colored according to their Lagrangian velocity,  $W_{Lag}$ , and the instantaneous streamwise Eulerian velocity,  $W_{Eu}$ , is presented in a plane through the center of the plume. Most noticeable is the great difference in the number of bubbles. The  $1$  mm bubble plume is narrower at the lower half of the tank, and the high concentration of particles stimulates plume wandering. In the  $1$  and  $2$  mm bubble diameter plumes, faster bubbles are located in the center of the plume and bubbles are slower toward the edge of the plume. As the bubble size increases, the plume becomes wider and instantaneous Eulerian velocities are reduced significantly.

The larger the bubble diameter the larger the buoyancy and the greater their Lagrangian velocity. However, for a given gas flow rate, there are many more smaller bubbles than larger ones (approx. 100 times more bubbles for the  $D_p = 1$  mm simulation than for  $D_p = 4$  mm). Furthermore, smaller bubbles have lower lift force (here the lift force acts in the horizontal plane, i.e., perpendicular to the streamwise direction) and hence they mainly



**Figure 1.** Instantaneous Eulerian and Lagrangian fields for the three uniform bubble size scenarios. The velocities are in  $m s^{-1}$ .



**Figure 2.** Half plume view of the bubble size arrangement within the plume for the multisize (MS) case.

remain clustered together around the center. Larger bubbles with greater lift force are pulled out of the center, resulting in a wider plume with larger gaps between the bubbles. The bunched rise of a large number of small bubbles concentrated in a narrow section of the plume induces higher velocities in the carrier phase than a few, spread out larger bubbles and allows them to rise faster than they would individually. When comparing the large bubbles' velocity with their surrounding carrier velocity (Figure 1), it is obvious why bigger bubbles yield a higher effective slip velocity, i.e., high Lagrangian and low Eulerian velocities. In contrast to that, smaller sized bubbles have a much lower slip velocity due to the relatively high speed of the Eulerian velocity.

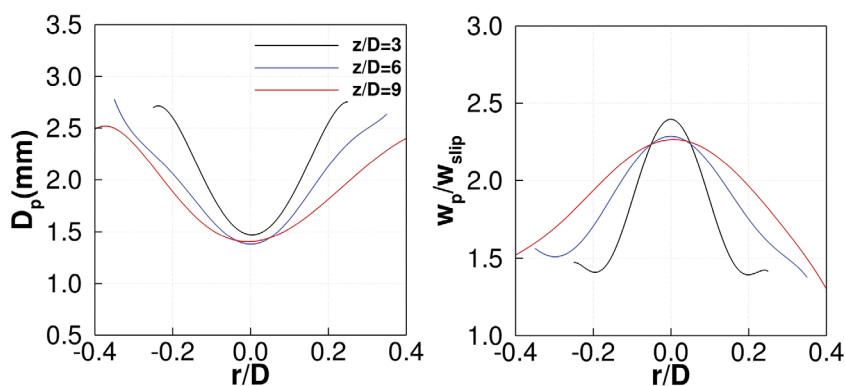
A visualization of the MS plume (cut in half) is provided in Figure 2 illustrating the distribution of bubble sizes within the plume. The figure depicts that the plume is well structured in terms of the bubble diameter with smaller bubbles (blue ones) located near the center of the plume and larger bubbles in the periphery, despite the fact that bubbles are released randomly over the diffuser area. This "self-arrangement" is due to the fact that smaller bubbles are subjected to lower lift force and hence they stay in the center, while larger bubbles experience larger lift and hence they are pulled outward.

Figure 2 is provided in Figure 3, which plots bubble-diameters,  $D_p$ , (left) and dimensionless bubble velocities,  $W_p/W_{slip}$ , (right) at selected elevations and as a function of the dimensionless distance ( $r/D$ ) from the center of the plume. The lines are polynomial fits to the data and they provide a good idea of the distribution pattern: smaller bubbles cluster in the center of the plume while the bigger ones move outward. The expression for the lift force helps understanding this behavior:

A quantitative confirmation of the observations of

$$F_{L,i} = -C_L \rho_{air} D_p (v_{p,i} - u_i) \times \omega_i \tag{16}$$

where  $C_L = 0.53$  is the lift coefficient for a sphere. The magnitude of the lift force depends directly on the particle's diameter. In the absence of prescribed lateral currents, this force is the main driver of the dispersion of bubbles in the radial direction. From animations, it is observed that bigger bubbles, when advected vertically



**Figure 3.** Radial distributions of (left) bubble diameters and (right) dimensionless streamwise Lagrangian velocities at three different heights for the multisize (MS) case.

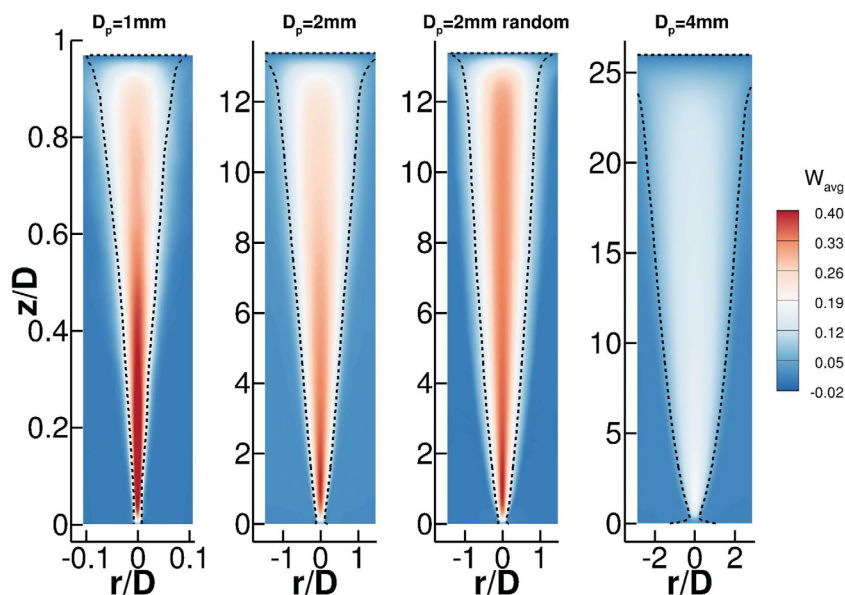


**Figure 4.** Time-averaged Eulerian streamwise velocity for the four proposed bubble-size scenarios. The dotted line indicates the edge of the velocity plume according to equation (9).

by the relatively strong current in the plume center, tend to meander in the radial axis until at some point they leave the core of the plume and continue their upward movement at the edge of the plume. Similarly, smaller bubbles have a much lower lift and hence lower capacity to move outward and hence they remain in the high momentum core. The right half of Figure 3 quantifies bubble velocities manifesting the trend that small bubbles move fast within the core and large bubbles move slower at the periphery of the plume.

Contours of the time-averaged streamwise velocity of the carrier phase are plotted for all four cases in Figure 4. The dotted lines represent the edge of the velocity plume determined with equation (9). Some of the aforementioned features are noticeable: the plume width increases with increasing bubble diameter while velocity magnitudes decrease. It is interesting to compare the uniform bubble size case with  $D_p = 2$  mm with the MS case, both having the same average bubble diameter. While the outer shape of both plumes is almost identical, the inner structure is not. The fluid velocity in the core of the MS plume remains quite high almost all the way to the water surface due to the clustering of small bubbles in the core. Consequently, the velocity gradient in the radial direction inside the plume is steeper for the MS case, but at the edge of the plume, the constant diameter case shows a higher gradient in the radial direction. The small-bubble plume is quite narrow and features high Eulerian velocities in the plume core and hence exhibits a steep velocity gradient in the radial direction. The large-bubble plume is very wide and is characterized by an almost uniform velocity distribution of low magnitude.

Based on the large-eddy simulations, the main integral properties of bubble plumes are extracted and compared with experimental data and integral plume model predictions with the aim to demonstrate the influence of the bubble size on the plume behavior. Figure 5 plots the results of the four simulations together with data from five different experimental studies and algebraic plume model predictions for the following three key properties of bubble plumes: plume radius ( $b_w$ ), time-averaged centerline streamwise velocity ( $W_c$ ), and mass flux ( $Q$ ). All these variables are nondimensionalized with  $D$  and  $w_{slip}$ .

From Figure 5, it can be seen that the simulations generally agree with experiments and integral model predictions. The good match of the LES-predicted  $b_w$  and  $Q$  for the 1 mm bubble plume with the integral models and the experiments is particularly interesting because, according to the most commonly accepted criterion, this plume has not yet reached the asymptotic region, which starts at approx.  $z/D > 5$ . The agreement of the 1 mm results is not so good regarding  $W_c$ , showing a good fit in terms of slope with Bombardelli's model but some overestimation. The reason for that may be in the release conditions, as the LES results and the experimental points tend to intersect as  $z/D$  increases. Noteworthy is that for larger bubbles (red and black lines) the LES results predict slightly different slopes than the integral plume models, in particular,

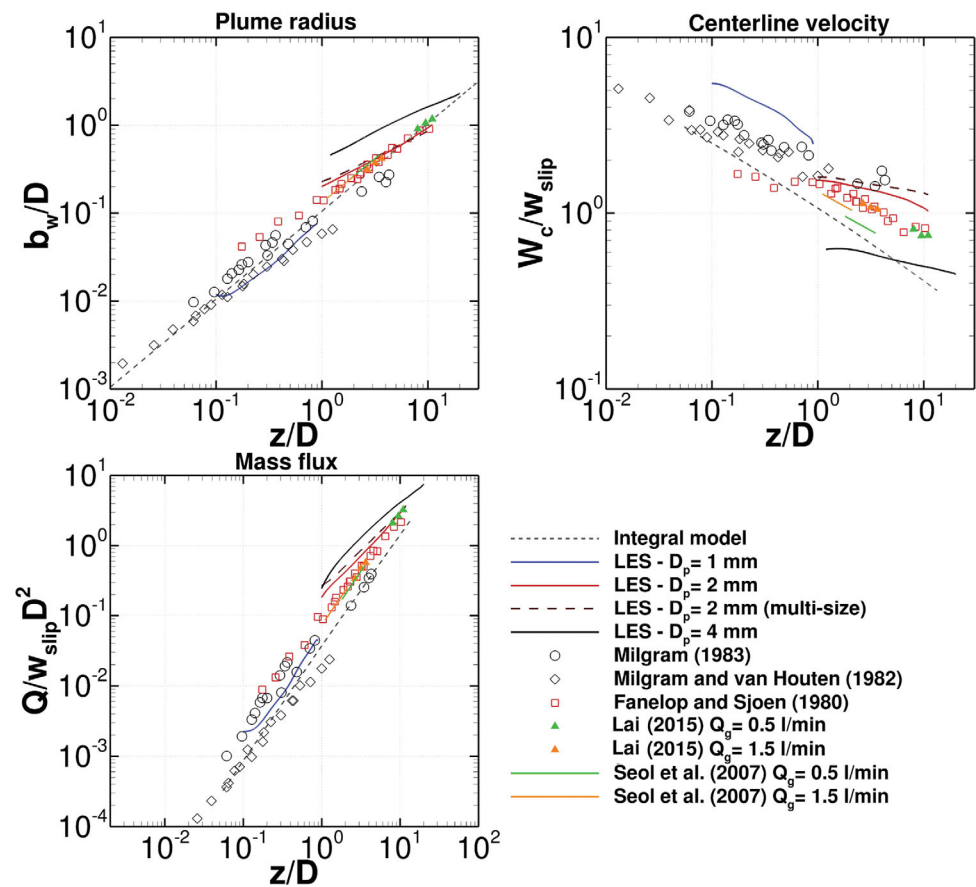


**Figure 5.** Numerical and experimental predictions of integral plume radius, centerline velocity, and mass flux. The data are taken from seven different experiments and two different integral models (see equations (10) and (11)), plus the LES for four different bubble size distributions (thicker lines).

for plume radius,  $b_w$ , and centerline velocity,  $W_c$ . Regarding the experiments, the comparison with the  $D_p = 4$  mm bubble LES results (black line) is difficult due to the few available data at high  $z/D$ . The match of the  $D_p = 2$  mm bubble (red line) and MS (dashed line) LES with the experiments is generally very good and some of the experimental data sets seem to agree with the LES in deviating from the integral model's slope (namely the measurements by *Fanelop and Sjoen* [1980] for  $b_w$  and the ones by *Milgram* [1983] for  $W_c$ ), suggesting that the bubble size does affect the integral quantities in mechanisms that are not accounted for by integral plume models. The results for the 2 mm and MS plumes are, as it should be expected, extremely similar, but the prediction of  $W_c$  reflects the aforementioned higher core velocity at increasing values of  $z/D$  in the MS case.

Figure 6 plots the entrainment,  $E$ , as a linear function of the centerline velocity,  $W_c$ , revealing the depth-averaged slope,  $\alpha$ , for each numerical experiment. Generally, the numerically predicted  $\alpha$  agrees well with the one from equation (14) for all plumes with constant bubble diameter, and agreement is almost perfect for the  $D_p = 2$  mm case. Clearly,  $\alpha$  decreases with decreasing bubble diameter, due to the narrowness of the plumes. The LES-predicted entrainment for the MS bubble plume is rather large ( $\alpha = 0.105$ ) and the discrepancy with the one given by equation (14) ( $\alpha = 0.075$ ) is remarkable. This suggests that the mechanism of entrainment is very much affected by the dynamic behavior of the bubbles at the edge of the plume. In both, the 4 mm case and the MS case large bubbles ( $D = 3\text{--}4$  mm) occupy the periphery of the plume (see Figures 2 and 3), smoothing the gradients in the radial direction between the plume and the surrounding fluid due to the wandering of these bigger bubbles. It can be concluded that the entrainment appears to be affected not only by the average bubble diameter, but also by the maximum bubble size in the plume.

Figure 7 shows the vertical distributions of the time-averaged and radially integrated momentum amplification factor  $\gamma$  (left) and the gas/velocity spread ratio  $\lambda$  (right) obtained by the LES. For  $\gamma$ , there are two sets of

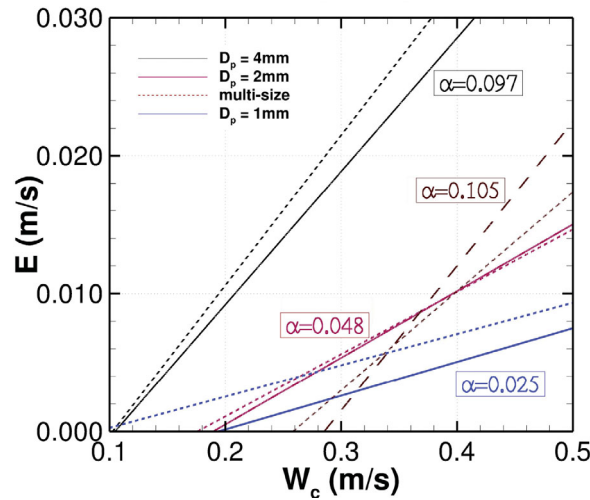


**Figure 6.** The relation between lateral inflow at the plume’s edge versus centerline velocity defines the entrainment rates for the four cases considered. Thick lines correspond to LES and thinner, dashed lines to *Seol et al.* [2007] algebraic model.

results: those that only consider the vertical contribution  $(\overline{w'w'} + \overline{W}^2)/\overline{W}^2$  to turbulence (solid and dashed lines) and those which also include the contribution of  $u'$  in the radial direction  $(\overline{w'w'} + \overline{u'u'} + \overline{W}^2)/\overline{W}^2$  (dash-dotted lines). In general, the inclusion of  $u'$  increases the value of  $\gamma$  by 12–20%. It does not change the overall distribution of  $\gamma$  but it exaggerates the peaks near the diffuser and the top of the tank for  $D_p = 1$  mm and  $D_p = 4$  mm. The low value of  $\gamma$  for the MS simulation is noteworthy. Lower velocity gradients observed in the MS case at the edge of the plume may play a role, as the peak of the Reynolds stresses  $\overline{u'_i u'_j}$  occurs at the interface between plume and ambient fluid. Overall, values for  $\gamma$  are between 1.2 and 1.5 when considering only the vertical momentum and between 1.4 and 1.9 when incorporating the U-component (except for the aforementioned MS case).

On the right side of Figure 7, the vertical distribution of  $\lambda$  is depicted. As the theory predicts, a smaller bubble size results in a higher spread ratio [see, for instance, *Liro et al.*, 1991]. Therefore, the bubble size plays a very important role in the quantification of  $\lambda$ . For instance,  $\lambda \approx 0.7$  on average for  $D_p = 4$  mm, while for  $D_p = 1$  mm  $\lambda > 1.0$ . In general, these results reflect Figures 1 and 4: once the plume is developed the radius of the bubble plume  $b_g$  is not strongly affected by the bubble size. However, the width of the entrained liquid plume, represented by  $b_w$  is rather sensitive to  $D_p$  (see Figures 4 and 5). Hence, larger bubbles lead to high  $b_w$  and, consequently, low  $\lambda$ . Again, an unexpected result is obtained from the MS simulation, which shows a very different behavior from its uniform size counterpart  $D_p = 2$  mm, being closer to  $D_p = 1$  mm. The results suggest that the spread ratio  $\lambda$  may be related to the length scale  $D$ . A greater  $D$  (94 cm for  $D_p = 1$  mm) implies a longer distance for the bubble plume to develop and this matches with values of  $\lambda$  greater than one. This relationship between  $D$  and  $\lambda$  is not reflected in the MS plume, due to the fact that the bubble-size distribution is not taken into account for the calculation of  $D$ .

**4.3. Influence of the Diffuser Width**

The initial plume width  $b_0$ , typically the diffuser width, together with the initial velocity  $w_0$ , provide the initial conditions for most integral plume models. *Wüest et al.* [1992] defined a densimetric Froude number that comprises both quantities and constitutes a simple way of providing realistic conditions to integral

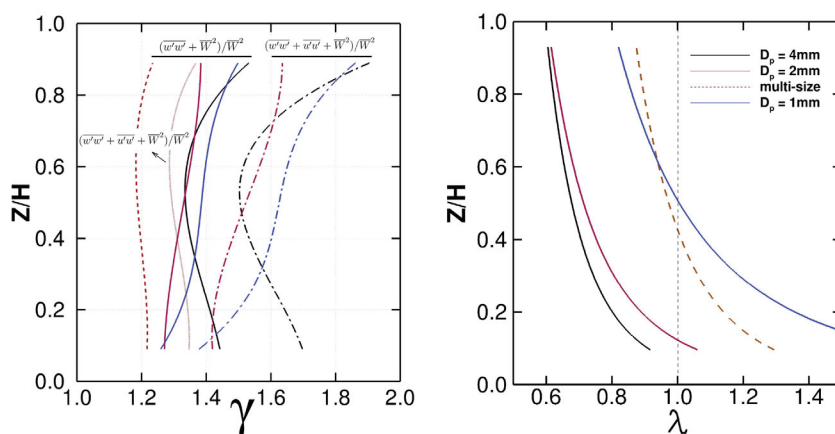


**Figure 7.** Vertical profiles of (left) the amplification factor ( $\gamma$ ) and (right) the spread ratio ( $\lambda$ ) for the four bubble size distributions considered.

**Table 2.** Initial Densimetric Bubble Froude Numbers for the Proposed Diffuser Diameters

	$b_0=1.5$ cm	$b_0=3$ cm	$b_0=6$ cm
$F_0$	0.74	1.04	1.48

flow rate is  $Q_g = 0.5$  L/min, the bubble diameter is  $D = 2$  mm, and the initial velocity of the bubbles at the diffuser is  $w_0 = w_{slip} = 24$  cm/s, providing initial densimetric Froude numbers which are listed in Table 2.

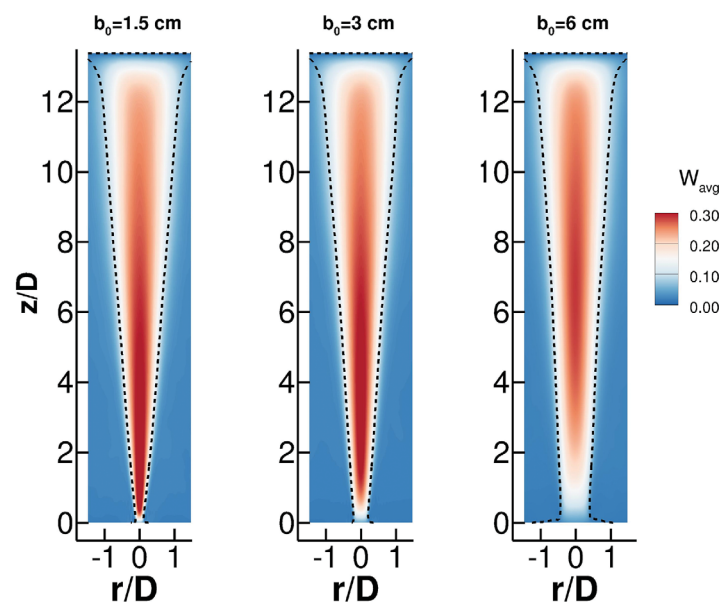
Figure 8 presents contours of the calculated time-averaged streamwise velocity and plume shapes in the symmetry plane. The different diffuser widths induce drastic differences in the velocity gradients at the release point. A high concentration of bubbles, i.e., small release area, triggers high velocities almost immediately at the diffuser. For wider diffusers, the velocities at the diffuser are fairly small and the high momentum plume core is formed only gradually, hence the area of highest time-averaged vertical velocity is found higher up in the plume than for narrow diffuser widths. For  $b_0 = 6$  cm, the adjustment zone (typically  $Z = 10b_0 = 60$  cm) reaches beyond the usual start of the asymptotic zone ( $Z = 5D = 34$  cm), and this is clearly reflected in Figure 8. However, the general shape of the plumes and their velocity magnitudes and distributions are very similar above  $z/D = 6$  irrespective of the diffuser width.

Figure 9 plots numerically and experimentally obtained bubble plume quantities: plume radius ( $b_w$ ), time-averaged centerline velocity ( $W_c$ ), and mass flux ( $Q$ ) together with predictions based on integral plume model equations (see equations (10) and (11)). The influence of the diffuser geometry is quite obvious, in particular, for wide diffusers. For  $z/D > 6$ , i.e., fully developed plume, the predicted quantities show reasonably good agreement with both experimental and integral plume model results, except, and as mentioned in conjunction with Figure 5, for the differences in slope with the integral model for the prediction of  $W_c$ . Larger diffuser diameter (and consequently larger densimetric Froude numbers) results in a delay in the plume attaining asymptotic behavior. This is most noticeable for the time-averaged streamwise centerline velocity  $W_c$ : for  $b_0 = 3$  cm, the velocity converges to a straight line around  $z/D = 3$  while for  $b_0 = 6$  cm only converges around  $z/D = 7$ .

The calculated entrainment coefficients are plotted in Figure 10. The LES and algebraic model show different responses to the changes in diffuser width. There is very good agreement in the prediction of the slope,  $\alpha$ , for the two extreme cases ( $b_0 = 1.5$  and 6 cm), while  $b_0 = 3$  cm shows a rather important discrepancy. In both models, the increase of the release area induces a lower entrainment. This seems to be caused by the

delay in the generation of the asymptotic region. However, while for Seol's model, there is a big shift in the prediction of  $\alpha$  between 1.5 and 3 cm, for LES it occurs between 3 and 6 cm, reflecting the short adjustment zone ( $Z \leq 10b_0$ ) observed in Figures 8 and 9.

Figure 11 presents the vertical distributions of  $\gamma$  (left) and  $\lambda$  (right) for the three different diffuser sizes. Regarding the momentum amplification factor ( $\gamma$ ), the ranges are between 1.2 and 1.4 when considering only the vertical fluctuations  $(\overline{w'w'} + \overline{W}^2)/\overline{W}^2$  (solid lines) and between 1.4 and 1.8 when incorporating the radial component  $(\overline{w'w'} + \overline{u'u'} + \overline{W}^2)/\overline{W}^2$  (dash-dotted lines). The resulting



**Figure 8.** Time-averaged Eulerian streamwise velocity for the three different diffuser sizes. The dotted line indicates the edge of the plume according to equation (9).

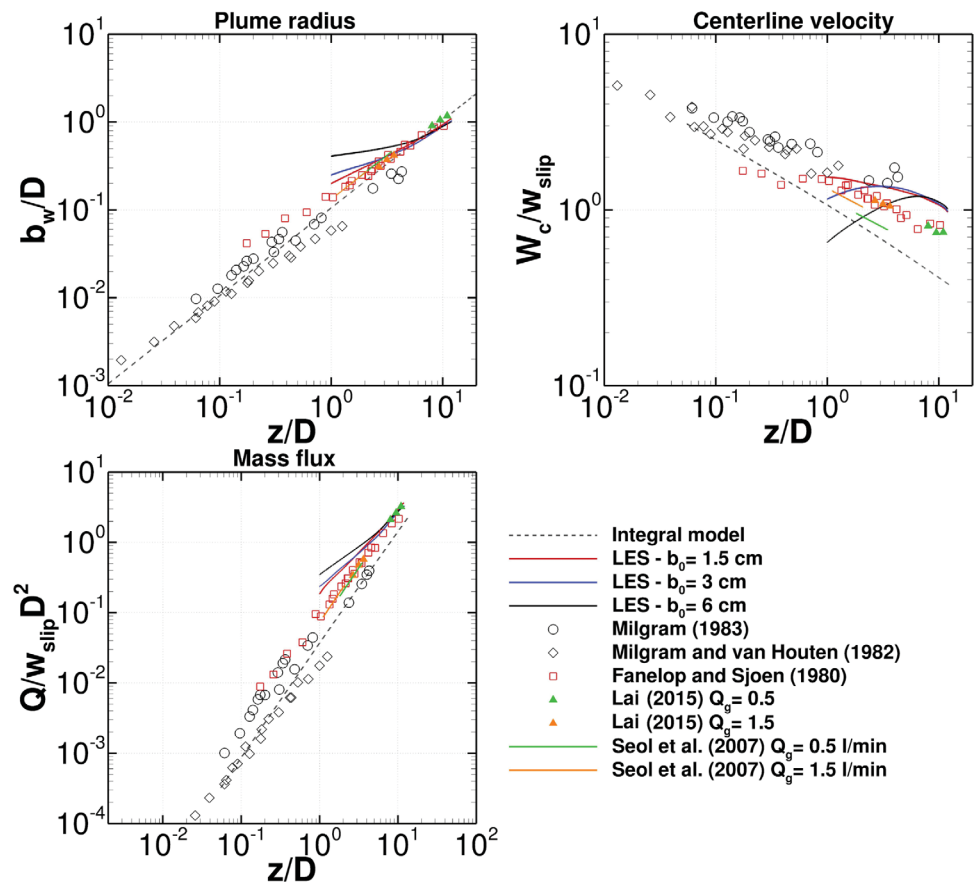


**Figure 9.** Numerical and experimental predictions of integral plume radius, centerline velocity, and mass flux. The data are taken from seven different experiments and two different integral models (see equations (10) and (11)), plus the LES for three different diffuser widths (thicker lines).

difference between these two approaches is approx. 20%, similar to the bubble-size cases. The value of  $\gamma$  is fairly constant for the case that only accounts for  $w'w'$ , except near the diffuser, and it is remarkable how the profiles become more curvy for  $b_0 = 3$  and 6 cm. The bigger release area appears to promote turbulence in the horizontal plane at various locations along the adjustment region ( $Z < 10b_0$ ).

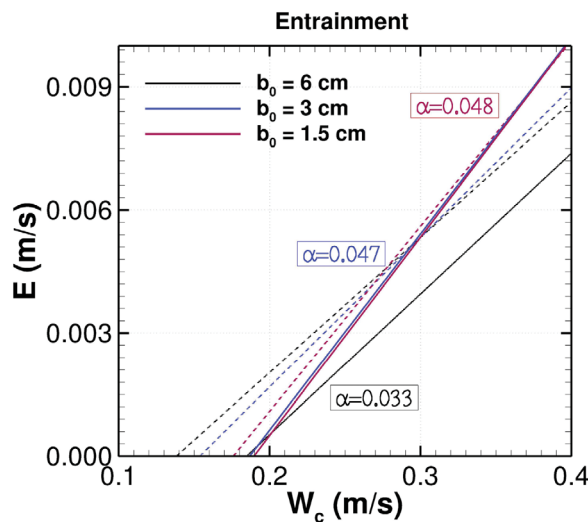


**Figure 10.** Lateral inflow at the plume's edge versus centerline velocity and entrainment rates for the three diffuser diameters. Thick lines correspond to LES and thinner, dashed lines to Seol et al. [2007] algebraic model.

For  $\lambda$ , the three profiles are fairly similar and they are all in the range of  $\lambda = 0.6-1$ . The two larger diffuser sizes (6 and 3 cm) follow almost identical curves and provide a higher  $\lambda$  than for  $b_0 = 1.5$  cm. The ratio between the bubble plume's width and the plume's momentum width (as defined in equation (9)) is fairly similar in the three scenarios. As  $b_w$  is very similar for the three cases (see Figures 8 and 9), greater  $\lambda$  for  $b_0 = 3$  and 6 cm suggests that the radius of the bubble plume  $b_g$  is smaller for the two large diffuser cases. This may be the result of the delayed plume development induced by the large diffusers which might eventually be corrected for longer plumes but this cannot be confirmed with the data available.

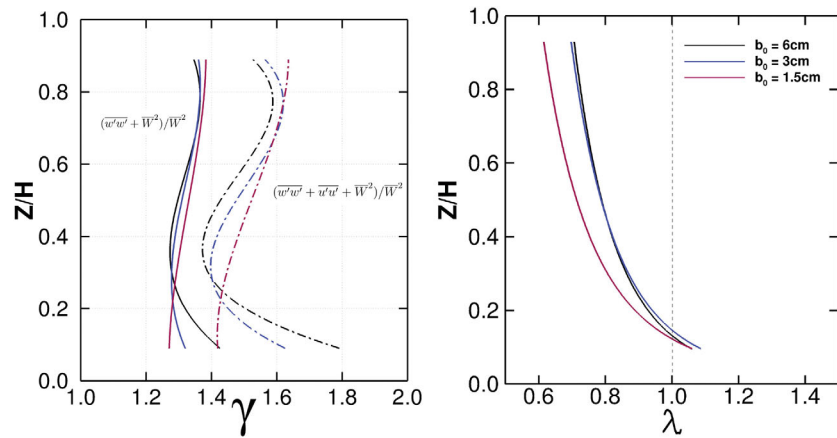


Figure 11. Vertical profiles of (left) the amplification factor ( $\gamma$ ) and (right) the spread ratio ( $\lambda$ ) for the three diffuser diameters considered.

#### 4.4. Influence of the Gas Flow Rate

The effect of two different gas flow rates, i.e., 0.5 and 1.5 L/min, on the integral behavior of the plume is analyzed. This implies a change in the number of bubbles to be released per time step, as it is reflected in Table 1. The bubble diameter is set to 2 mm and the diffuser width to 1.5 cm for both simulations.

Figure 12 shows the time-averaged Eulerian velocity field (left) and instantaneous Lagrangian and Eulerian streamwise velocity fields (right) for the two cases. The magnitude of the time-averaged velocity for the 1.5 L/min flow rate is about a 40% higher than for the lower  $Q_g$ , due to the presence of many more bubbles and, therefore, a higher buoyancy in the plume. A stronger gas flow rate also implies more wandering (meandering) of the plume as is visible in the instantaneous plots. The shape and width of the plumes are almost identical; the 1.5 L/min case is slightly wider but there is no significant difference.

Figure 13 plots plume radius ( $b_w$ ), time-averaged centerline velocity ( $W_c$ ), and mass flux ( $Q$ ) for the two simulations together with experimental data sets and predictions from integral plume models (see equations

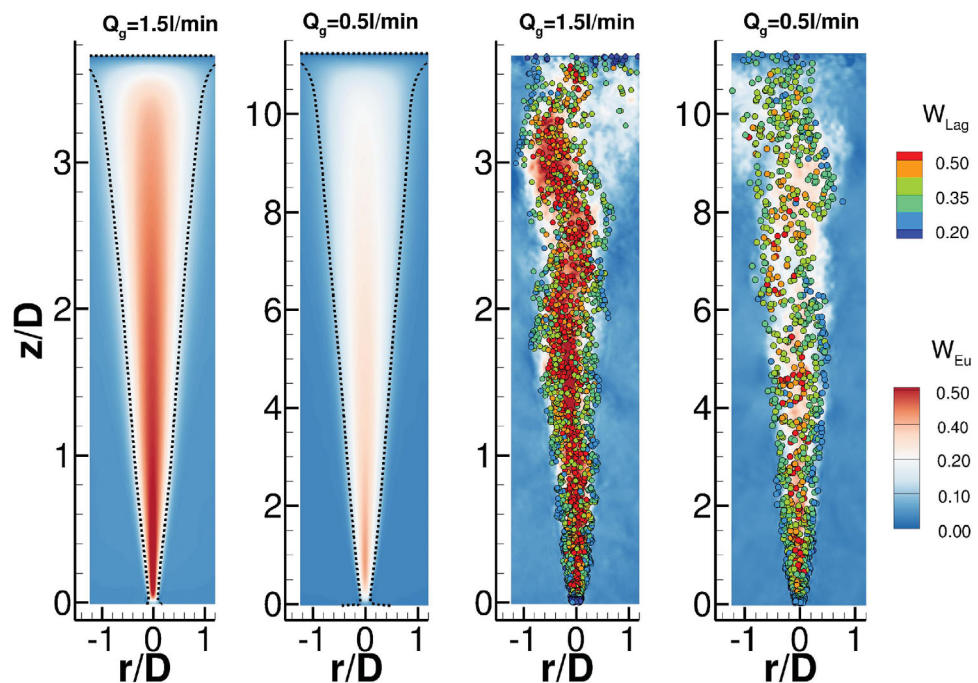
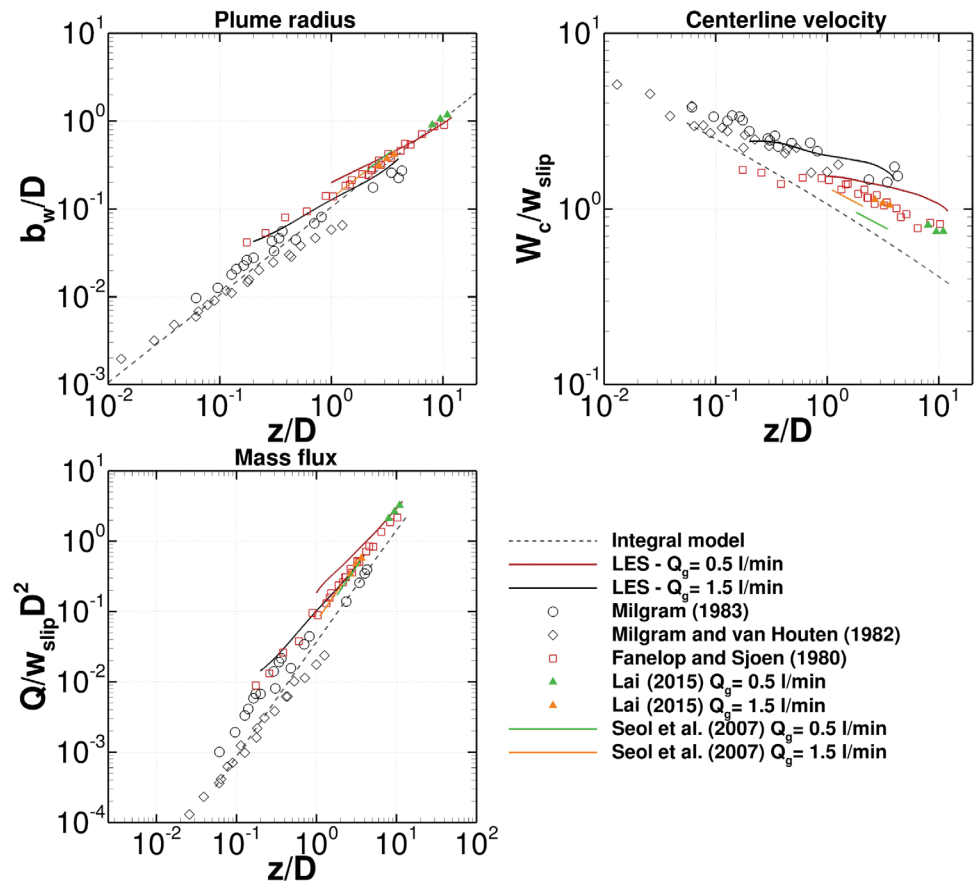
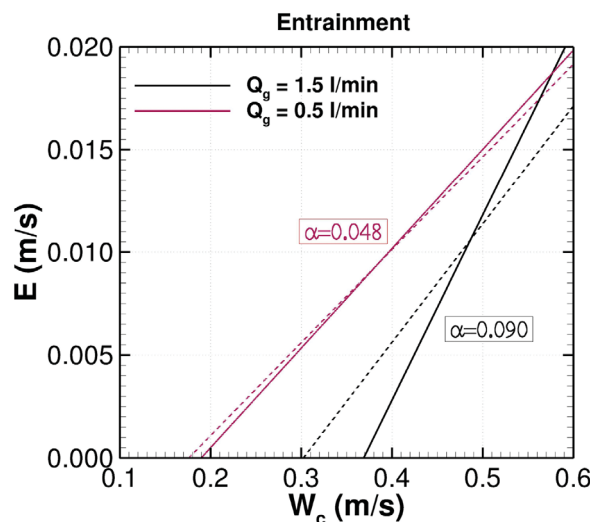


Figure 12. (left) Time-averaged Eulerian streamwise velocity and (right) instantaneous Eulerian and Lagrangian velocities for the two different gas flow rates simulated. The dotted line indicates the edge of the plume according to equation (9).



**Figure 13.** Numerical and experimental predictions of integral plume radius, centerline velocity, and mass flux. The data are taken from seven different experiments and two different integral models (see equations (10) and (11)), plus the LES for two different gas discharges (thicker lines).

(10) and (11)). The simulated quantities match quite well the experimental data sets in particular for the higher gas flow rate. The agreement with the data by *Lai* [2015] and *Seol et al.* [2007] is not necessarily surprising given that gas flow rates and geometrical conditions are identical, however, very good agreement is



**Figure 14.** Lateral inflow at the plume's edge versus centerline velocity and entrainment rates for the two different gas discharges. Thick lines correspond to LES and thinner, dashed lines to *Seol et al.* [2007] algebraic model.

also obtained with the other data sets. Unlike the bubble size, the direct influence of the gas flow rate seems to be very well depicted by the integral models.

The effect of gas flow rate on the entrainment coefficient is appreciated from Figure 14 which plots  $E$  as a function of centerline velocity  $W_c$ . As before, the match between the integral model and LES predictions is very good for the lower gas flow rate, however, for the higher gas flow rate, there is disagreement about the entrainment coefficient between the LES and the algebraic model. While *Seol's* model suggest that 0.5 and 1.5 L/min flow rates should yield similar coefficients, LES indicates a substantially higher entrainment at higher flow rate. The slope of the higher discharge line is almost double than the lower one, likely the result of increased wandering of the plume leading to a higher lateral inflow.

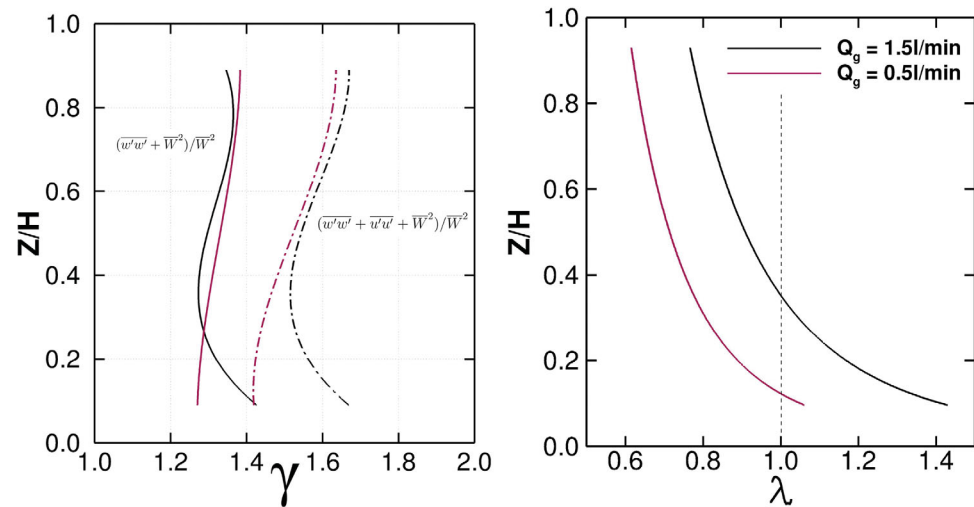


**Figure 15.** Vertical profiles of (left) the amplification factor ( $\gamma$ ) and (right) the spread ratio ( $\lambda$ ) for the two gas flow rates considered.

Figure 15 represents the vertical distributions of the momentum amplification factor  $\gamma$  (left) and the gas-to-velocity spread ratio  $\lambda$  (right) estimated by the LES. The values of  $\gamma$  range between 1.2 and 1.4 and 1.4 and 1.7, respectively. It is interesting to note that the two cases provide very close results except near the diffuser. It seems that the higher gas flow rate induces higher turbulence near the release point, but the ratio between  $\overline{u'_i u'_j}$  and  $\bar{W}^2$  balances out around  $Z/H \approx 0.3$  for the vertical turbulence and at  $Z/H \approx 0.5$  for  $u' + w'$ .

Higher values of  $\lambda$  are observed for the  $Q_g = 1.5$  L/min case.  $\lambda$  is approximately 30% greater than for the  $Q_g = 0.5$  L/min simulation. Similar to the  $D_p = 1$  mm plume, a significant part of the  $Q_g = 1.5$  L/min plume, for which  $D$  is 4 times larger than for  $Q_g = 0.5$  L/min, is in the  $\lambda > 1$  region suggesting that  $\lambda$  can complement  $D$  as an indicator of plume development.

## 5. Conclusions

LES was employed to investigate the impact of bubble size, diffuser diameter and flow rate on the dynamics of a bubble plume and in particular on its main integral properties and the critical empirical coefficients of the governing plume model equations.

Three uniform-bubble-size plumes with bubble diameters 1, 2, and 4 mm as well as one multi-diameter case (bubble diameters ranging from 0.75 to 3.25 mm) have been simulated. Smaller bubbles generate narrower plumes and induce high velocities in the carrier phase, while larger bubbles lead to wider plumes with a rather uniform velocity distribution and lower in magnitude than the small-bubble plume. In the multi-diameter bubble plume, the bubbles arrange themselves according to their diameter: small bubbles cluster in the center of the plume and larger move toward the periphery of the plume due to their larger lift force. The bubble size has a moderate impact on the plume radius, centerline velocity, and mass flux, and overall the behavior is according to integral plume model predictions. The smaller the bubbles the better the match; however, the results also show that larger bubbles induce a higher entrainment rate, which is in agreement with *Seol et al.'s* [2007] model. The multidiameter plume entrainment differs significantly from the algebraic entrainment predictions, suggesting that the entrainment is not only governed by the medium bubble diameter but also by the maximum bubble diameter. The momentum amplification coefficient appears to be affected by bubble size and distribution and the results show that the contribution of the turbulence in the horizontal plane to the momentum transport can be significant. The gas-to-velocity spread ratio is very sensitive to the bubble size, showing values of  $\lambda > 1$  for small bubbles in the plume's core (1 mm and multidiameter cases). The results suggest a correlation between the spread ratio and the plume development distance,  $D$ .

Three diffuser widths have been considered, i.e., 1.5, 3, and 6 cm to study the effect of release area on the bubble plume. It has been shown that the diffuser diameter has a big impact on the plume's dynamics near the release point and on the establishment of the asymptotic region. For the large diffuser, the asymptotic behavior is not attained until  $z/D=7$ , surpassing the lower limit suggested by *Bombardelli et al.* [2007]. The plume's width, shape, and centerline velocity are not affected very much by the diffuser size. On the other hand, the entrainment process seems to be sensitive to the diffuser width: larger diffusers result in lower entrainment rates. The increasing release area induces a shift in the entrainment rate which deviates from the integral plume model predictions. The momentum amplification factor appears affected by the diffuser width; large diffusers seem to induce higher levels of turbulence near the release point particularly in the radial direction. The gas-to-velocity spread ratio seems quite insensitive to the diffuser size in the vicinity of the diffuser itself.

Two gas flow rates of 0.5 and 1.5 L/min have been simulated for constant bubble and diffuser sizes. The higher flow rate does not seem to change drastically the shape of the plume, but the presence of more bubbles induces a higher momentum flux inside the bubble column. Observations have revealed that the meandering motion of the plume is more pronounced for the higher flow rate. In terms of the prediction of the integral plume radius, centerline velocity and mass flux, the flow rate does not have a significant effect. Entrainment rates however appear to depend on the gas flow rate. While the *Seol et al.* [2007] model predicts fairly similar entrainment coefficients for the two flow rates, the LES results suggests a higher entrainment for 1.5 L/min. This may be due to the more pronounced meandering motion of the plume for higher gas flows. The momentum amplification factor only exhibited sensitivity to the gas flow rate on the lower part of the plume. The gas-to-velocity spread ratio is considerably and consistently higher for the high gas flow rate and the development length of the plume appears to reflect this in the same way as for the small bubble diameter plume.

#### Acknowledgments

This research was made possible by a grant from The Gulf of Mexico Research Initiative. The numerical code used for this research is publicly available through the Gulf of Mexico Research Initiative Information & Data Cooperative (GRINDC) at <https://data.gulfresearchinitiative.org> (doi:10.7266/N76W980Z). The simulations were performed in the computational facilities of the Advanced Research Computing at Cardiff (ARCCA) Division, Cardiff University.

#### References

- Asaeda, T., and J. Imberger (1993), Structure of bubble plumes in linearly stratified environments, *J. Fluid Mech.*, 249(1), 35–57, doi:10.1017/s0022112093001065.
- Bai, J., H. Fang, and T. Stoesser (2013), Transport and deposition of fine sediment in open channels with different aspect ratios, *Earth Surf. Processes Landforms*, 38(6), 591–600.
- Bombardelli, F., G. Buscaglia, C. Rehmman, L. Rincón, and M. García (2007), Modeling and scaling of aeration bubble plumes: A two-phase flow analysis, *J. Hydraul. Res.*, 45(5), 617–630.
- Bomminayuni, S., and T. Stoesser (2011), Turbulence statistics in an open-channel flow over a rough bed, *J. Hydraul. Eng.*, 137(11), 1347–1358.
- Bunner, B., and G. Tryggvason (2002), Dynamics of homogeneous bubbly flows part 1. Rise velocity and microstructure of the bubbles, *J. Fluid Mech.*, 466, 17–52, doi:10.1017/s0022112002001179.
- Buscaglia, G. C., F. A. Bombardelli, and M. H. García (2002), Numerical modeling of large-scale bubble plumes accounting for mass transfer effects, *Int. J. Multiphase Flow*, 28(11), 1763–1785, doi:10.1016/s0301-9322(02)00075-7.
- Cederwall, K., and J. D. Ditmars (1970), Analysis of air-bubble plumes, *Rep. KH-R-24*, Calif. Inst. of Technol., W. M. Keck Lab. of Hydraul. and Water Resour., Pasadena, CA.
- Chan, G. K. Y., A. C. Chow, and E. E. Adams (2014), Effects of droplet size on intrusion of sub-surface oil spills, *Environ. Fluid Mech.*, 15(5), 959–973, doi:10.1007/s10652-014-9389-5.
- Clift, R., J. R. Grace, and M. E. Weber (1978), *Bubbles, Drops, and Particles*, Academic Press, N. Y.
- Crouse, B. C. (2000), Modeling buoyant droplet plumes in a stratified environment, PhD thesis, Mass. Inst. of Technol., Cambridge.
- Darmana, D., N. Deen, and J. Kuipers (2006), Parallelization of an Euler–Lagrange model using mixed domain decomposition and a mirror domain technique: Application to dispersed gas–liquid two-phase flow, *J. Comput. Phys.*, 220(1), 216–248, doi:10.1016/j.jcp.2006.05.011.
- Deen, N., T. Solberg, and B. Hjertager (2001), Large eddy simulation of the gas–liquid flow in a square cross-sectioned bubble column, *Chem. Eng. Sci.*, 56(21–22), 6341–6349, doi:10.1016/s0009-2509(01)00249-4.
- Deen, N., M. van Sint Annaland, and J. Kuipers (2004), Multi-scale modeling of dispersed gas–liquid two-phase flow, *Chem. Eng. Sci.*, 59(8–9), 1853–1861, doi:10.1016/j.ces.2004.01.038.
- Delnoij, E., F. Lammers, J. Kuipers, and W. van Swaaij (1997), Dynamic simulation of dispersed gas-liquid two-phase flow using a discrete bubble model, *Chem. Eng. Sci.*, 52(9), 1429–1458, doi:10.1016/s0009-2509(96)00515-5.
- Dhotre, M. T., B. Ničeno, B. L. Smith, and M. Simiano (2009), Large-eddy simulation (les) of the large scale bubble plume, *Chem. Eng. Sci.*, 64(11), 2692–2704, doi:10.1016/j.ces.2009.02.040.
- Dhotre, M. T., N. G. Deen, B. Ničeno, Z. Khan, and J. B. Joshi (2013), Large eddy simulation for dispersed bubbly flows: A review, *Int. J. Chem. Eng.*, 2013, 1–22, doi:10.1155/2013/343276.
- Esmaeili, A., and G. Tryggvason (1998), Direct numerical simulations of bubbly flows. Part 1. Low Reynolds number arrays, *J. Fluid Mech.*, 377, 313–345, doi:10.1017/s0022112098003176.
- Fabregat, A., W. K. Dewar, T. M. Özgökmen, A. C. Poje, and N. Wienders (2015), Numerical simulations of turbulent thermal, bubble and hybrid plumes, *Ocean Modell.*, 90, 16–28, doi:10.1016/j.ocemod.2015.03.007.
- Fannelop, T. K., and K. Sjoen (1980), Hydrodynamics of underwater blowouts, *Norwegian Maritime Research*, 4, 17–33.
- Fraga, B., T. Stoesser, C. K. C. Lai, and S. Socolofsky (2016), A LES-based Eulerian-Lagrangian approach to predict the dynamics of bubble plumes, *Ocean Modell.*, 97, 27–36.
- Hu, G., and I. Celik (2008), Eulerian–Lagrangian based large-eddy simulation of a partially aerated flat bubble column, *Chem. Eng. Sci.*, 63(1), 253–271, doi:10.1016/j.ces.2007.09.015.
- Kara, S., T. Stoesser, and T. W. Sturm (2012), Turbulence statistics in compound channels with deep and shallow overbank flows, *J. Hydraul. Res.*, 50(5), 482–493.

- Kara, S., T. Stoesser, T. W. Sturm, and S. Mulahasan (2015), Flow dynamics through a submerged bridge opening with overtopping, *J. Hydraul. Res.*, *53*(2), 282–294.
- Kim, D., J. H. Kim, and T. Stoesser (2013), The effect of baffle spacing on hydrodynamics and solute transport in serpentine contact tanks, *J. Hydraul. Res.*, *51*(5), 558–568.
- Kim, S., and T. Stoesser (2011), Closure modeling and direct simulation of vegetation drag in flow through emergent vegetation, *Water Resour. Res.*, *10*, W10511, doi:10.1029/2011WR010561.
- Kitagawa, A., Y. Murai, and F. Yamamoto (2001), Two-way coupling of Eulerian–Lagrangian model for dispersed multiphase flows using filtering functions, *Int. J. Multiphase Flow*, *27*(12), 2129–2153, doi:10.1016/S0301-9322(01)00040-4.
- Kobus, H. (1968), Analysis of the flow induced by air-bubble systems, paper presented at 11th International Conference in Coastal Engineering, Am. Soc. of Civ. Eng., Reston, Va.
- Lai, C. K. C. (2015), An analysis of bubble plumes in unstratified stagnant water, PhD thesis, Tex. A&M Univ., College Station, Tex.
- Liro, C. R., E. E. Adams, and H. J. Herzog (1992), Modeling the release of CO<sub>2</sub> in the deep ocean, *Energy Conversion and Management*, *33*(5–8), 667–674.
- Lu, J., A. Fernandez, and G. Tryggvason (2005), The effect of bubbles on the wall drag in a turbulent channel flow, *Phys. Fluids*, *17*(9), 95–102, doi:10.1063/1.2033547.
- Martinez Mercado, J., D. Chehata Gomez, D. van Gils, C. Sun, and D. Lohse (2010), On bubble clustering and energy spectra in pseudo-turbulence, *J. Fluid Mech.*, *650*, 287–306, doi:10.1017/S0022112009993570.
- Mazzitelli, I., and D. Lohse (2009), Evolution of energy in flow driven by rising bubbles, *Phys. Rev. E*, *79*(6), 066317, doi:10.1103/PhysRevE.79.066317.
- Mcdougall, T. J. (1978), Bubble plumes in stratified environments, *J. Fluid Mech.*, *85*(4), 655–672, doi:10.1017/S0022112078000841.
- McGinnis, D. F., and J. C. Little (2002), Predicting diffused-bubble oxygen transfer rate using the discrete-bubble model, *Water Res.*, *36*(18), 4627–4635, doi:10.1016/S0043-1354(02)00175-6.
- McGinnis, D. F., A. Lorke, A. West, A. Stckli, and J. C. Little (2004), Interaction between a bubble plume and the near field in a stratified lake, *Water Resour. Res.*, *40*, W10206, doi:10.1029/2004WR003038.
- Milelli, M., B. Smith, and D. Lakehal (2001), Large-eddy simulation of turbulent shear flows laden with bubbles, in *Direct and Large-Eddy Simulation IV, ERCOFTAC Ser.*, vol. 8, edited by B. Geurts, R. Friedrich, and O. Mtais, pp. 461–470, Springer, Dordrecht, Netherlands, doi:10.1007/978-94-017-1263-7-55.
- Milgram, J. (1983), Mean flow in round bubble plumes, *J. Fluid Mech.*, *133*, 345–376.
- Milgram, J., and R. J. van Houten (1982), Plumes from sub-sea well blowouts, in *Proceedings of the 3rd International Conference BOSS*, vol. 1, pp. 659–684, Hemisphere, N. Y.
- Morton, B., G. Taylor, and J. Turner (1956), Turbulent gravitational convection from maintained and instantaneous sources, in *Proc. R. Soc. London, Ser. A*, *234*, 1–23.
- Ničeno, B., M. Boucker, and B. L. Smith (2009), Euler-Euler large eddy simulation of a square cross-sectional bubble column using the Neptune-CFD code, *Sci. Technol. Nucl. Installations*, *2009*, 1–8, doi:10.1155/2009/410272.
- North, E. W., E. E. Adams, Z. Schlag, C. R. Sherwood, R. He, K. H. Hyun, and S. A. Socolofsky (2011), Simulating oil droplet dispersal from the Deepwater Horizon spill with a Lagrangian approach, in *Monitoring and Modeling the Deepwater Horizon Oil Spill: A Record-Breaking Enterprise*, *Geophys. Monogr. Ser.*, vol. 195, edited by Y. Liu et al., pp. 217–226, AGU, Washington, D. C.
- Papanicolaou, A. N., C. M. Kramer, A. G. Tsakiris, T. Stoesser, S. Bomminayuni, and Z. Chen (2012), Energy spectra and bubble velocity distributions in pseudo-turbulence: Numerical simulations vs. experiments, *Acta Geophys.*, *60*(6), 1502–1546.
- Roghair, I., J. M. Mercado, M. V. Sint Annaland, H. Kuipers, C. Sun, and D. Lohse (2011), Energy spectra and bubble velocity distributions in pseudo-turbulence: Numerical simulations vs. experiments, *Int. J. Multiphase Flow*, *37*(9), 1093–1098, doi:10.1016/j.ijmultiphaseflow.2011.07.004.
- Rouse, H., C. Yih, and H. Humphreys (1952), Gravitational convection from a boundary source, *Tellus*, *4*(3), 201–210.
- Seol, D.-G., T. Bhaumik, C. Bergmann, and S. A. Socolofsky (2007), Particle image velocimetry measurements of the mean flow characteristics in a bubble plume, *J. Eng. Mech.*, *133*(6), 665–676, doi:10.1061/(ASCE)0733-9399(2007)133:6(665).
- Socolofsky, S. A., and E. E. Adams (2002), Multi-phase plumes in uniform and stratified crossflow, *J. Hydraul. Res.*, *40*(6), 661–672, doi:10.1080/00221680209499913.
- Socolofsky, S. A., and E. E. Adams (2003), Liquid volume fluxes in stratified multiphase plumes, *J. Hydraul. Eng.*, *129*(11), 905–914, doi:10.1061/(ASCE)0733-9429(2003)129:11(905).
- Socolofsky, S. A., and E. E. Adams (2005), Role of slip velocity in the behavior of stratified multiphase plumes, *J. Hydraul. Eng.*, *131*(4), 273–282, doi:10.1061/(ASCE)0733-9429(2005)131:4(273).
- Socolofsky, S. A., B. C. Crouse, and E. E. Adams (2002), Multiphase plumes in uniform, stratified, and flowing environments, in *Environmental Fluid Mechanics Theories and Applications*, pp. 85–125, ASCE/Fluids Committee.
- Socolofsky, S. A., T. Bhaumik, and D.-G. Seol (2008), Double-plume integral models for near-field mixing in multiphase plumes, *J. Hydraul. Eng.*, *134*(6), 772–783, doi:10.1061/(ASCE)0733-9429(2008)134:6(772).
- Sokolichin, A., G. Eigenberger, A. Lapin, and A. Lbert (1997), Dynamic numerical simulation of gas-liquid two-phase flows Euler/Euler versus Euler/Lagrange, *Chem. Eng. Sci.*, *52*(4), 611–626, doi:10.1016/S0009-2509(96)00425-3.
- Stoesser, T. (2014), Large-eddy simulation in hydraulics: Quo vadis?, *J. Hydraul. Res.*, *52*(4), 441–452, doi:10.1080/00221686.2014.944227.
- Sungkorn, R., J. Derksen, and J. Khinast (2011), Modeling of turbulent gas-liquid bubbly flows using stochastic Lagrangian model and lattice-Boltzmann scheme, *Chem. Eng. Sci.*, *66*(12), 2745–2757, doi:10.1016/j.ces.2011.03.032.
- Turner, J. S. (1986), Turbulent entrainment: the development of the entrainment assumption, and its application to geophysical flows, *J. Fluid Mech.*, *173*(1), 431–471, doi:10.1017/S0022112086001222.
- Wüest, A., N. H. Brooks, and D. M. Imboden (1992), Bubble plume modeling for lake restoration, *Water Resour. Res.*, *28*, 3235–3250, doi:10.1029/92WR01681.
- Yang, X., X. Zhang, Z. Li, and G.-W. He (2009), A smoothing technique for discrete delta functions with application to immersed boundary method in moving boundary simulations, *J. Comput. Phys.*, *228*(20), 7821–7836, doi:10.1016/j.jcp.2009.07.023.
- Yapa, P. D., L. Zheng, and K. Nakata (1999), Modeling underwater oil/gas jets and plumes, *J. Hydraul. Eng.*, *125*(5), 481–491, doi:10.1061/(ASCE)0733-9429(1999)125:5(481).
- Yujie, Z., L. Mingyan, X. Yonggui, and T. Can (2012), Three-dimensional volume of fluid simulations on bubble formation and dynamics in bubble columns, *Chem. Eng. Sci.*, *73*, 55–78, doi:10.1016/j.ces.2012.01.012.